

Article

Effect of Annealing on the Microstructure and SERS Performance of Mo-48.2% Ag Films

Haoliang Sun ^{1,2,*}, Xinxin Lian ^{1,†}, Yuanjiang Lv ¹, Yuanhao Liu ¹, Chao Xu ¹, Jiwei Dai ¹, Yilin Wu ¹ and Guangxin Wang ¹

¹ School of Materials Science and Engineering, Henan University of Science and Technology, Luoyang 471023, China; lianxinxincn@163.com (X.L.); lyj_solovely@163.com (Y.L.); yh088232@163.com (Y.L.); chaoxu811@163.com (C.X.); dai978335921@163.com (J.D.); wyl1593571232@163.com (Y.W.); wgx58@126.com (G.W.)

² Collaborative Innovation Center of Nonferrous Metals Henan Province, Luoyang 471003, China

* Correspondence: sunhlwm@163.com

† These authors have contributed equally to this work.

Received: 21 August 2020; Accepted: 18 September 2020; Published: 22 September 2020



Abstract: Mo-48.2% Ag films were fabricated by direct current (DC) magnetron sputtering and annealed in an argon atmosphere. The effects of annealing on the surface morphology, resistivity and surface-enhanced Raman scattering (SERS) performance of Mo-48.2% Ag films were investigated. Results show a mass of polyhedral Ag particles grown on the annealed Mo-48.2% Ag films' surface, which are different from that of as-deposited Mo-Ag film. Moreover, the thickness and the resistivity of Mo-48.2% Ag films gradually decrease as the annealing temperature increases. Furthermore, finite-difference time-domain (FDTD) simulations proved that the re-deposition Ag layer increases the "hot spots" between adjacent Ag nanoparticles, thereby greatly enhancing the local electromagnetic (EM) field. The Ag layer/annealed Mo-48.2% Ag films can identify crystal violet (CV) with concentration lower than 5×10^{-10} M (1 mol/L = 1 M), which indicated that this novel type of particles/films can be applied as ultrasensitive SERS substrates.

Keywords: Mo-48.2% Ag film; anneal; polyhedral Ag particles; SERS

1. Introduction

Surface-enhanced Raman scattering (SERS) is a super-sensitive detection technique [1,2], which has become a powerful spectral method for identification and quantitative analysis of compounds [3]. However, the preparation of high-performance SERS substrate becomes crucial to the practical application of SERS technology due to the weak Raman signal [4,5]. The performance of SERS depends largely on the surface properties and materials of SERS substrates [6]. SERS substrates are usually made of noble metal (Ag, Au, Cu) nanomaterials, which can excite local surface plasmon resonance (LSPR) to generate strong extinction and scattering spectra [7]. In particular, SERS substrates composed of Ag nanostructures exhibit better SERS performance [8].

Currently, various Ag nanostructures, such as nanospheres [9], cubic [10], flower-like [11], triangles [12], nanowires [13], nanoneedles [14], nanorods [15], nanoshells [16], nanoclusters [17] and other polyhedral shapes [18], have been made by "top-down" or "bottom-up" assembly methods [19]. "Top-down" lithography with high-reproducibility and large-scale manufacturing has been widespread applied in industry [20]. However, the complicated synthesis or fabrication procedures cause inconvenience in common analysis [21]. Therefore, the relatively "bottom-up" method has developed greatly in recent years, for example, the solvent evaporation method [22], the electrodeposition method [23], Langmuir–Blodgett technology [24], the self-assembly method [25]

and other methods [26]. The self-assembly technology, in particular, makes use of the surface functional groups, potential, morphology and other characteristics of nanostructures to spontaneously form dense and controllable nanostructures [27]. So far, it is still a focus in the research field of SERS substrate structures.

It is imperative to manufacture highly efficient SERS-active substrates in order to detect and identify trace harmful substances accurately and efficiently. Based on previous studies on the as-deposited Mo-Ag films and the annealed Ag-Zr films [28–30], plenty of self-formed Ag particles were found on the films' surface, which leads to a strong Raman response. As is well known, annealing has an important influence on the microstructure, residual stress of the film. Therefore, we planned to adjust the particle size, morphology and quantity of self-formed Ag particles on the Mo-48.2% Ag films by annealing to obtain a more sensitive SERS performance.

2. Materials and Methods

Mo-48.2% Ag films were prepared by a direct current (DC) magnetron sputtering system (JCP-350). The composite targets consisted of a \varnothing 50 mm \times 4 mm Mo target (99.99%) and four Ag sheets (5 mm \times 5 mm \times 1 mm) sputtered in high-purity argon (99.9999%).

Flexible polyimide (PI) substrates were cleaned with acetone, deionized water and ethanol for 15 min [28]. The pressure of the deposition chamber was pumped to 5×10^{-4} Pa, and pure argon was introduced to achieve deposition pressure (0.5 Pa). Sputtering power was controlled at about 100 W and pre-sputtered for 3 min [29]. Annealing was carried out at 160–360 °C, kept for 60 min in an argon atmosphere, and cooled in the furnace. Additionally, the annealed Mo-48.2% Ag films' surface was covered with an Ag layer under the same experimental parameters as the Mo-48.2% Ag film.

The morphology, composition and phase of Mo-48.2% Ag films were characterized through field-emission scanning electron microscope (FE-SEM, JSM 7800, JEOL Ltd., Tokyo, Japan) with energy-dispersive spectroscopy (EDS) and X-ray diffraction (XRD, Bruker-AXS D8 Advance, SHIMADZU LIMITED, Kyoto, Japan). The resistivity of the Mo-48.2% Ag film was characterized by four-point probe resistance (RTS-8) and the 2D electric field distribution was simulated by the finite-difference time-domain (FDTD) method. The SERS signals of crystal violet (CV, Sinopharm Chemical Reagent Co., Ltd., Beijing, China) on the Mo-48.2% Ag films were characterized by Raman spectrometer (Invia Raman Microscope, Renishaw, Cambridge, UK).

3. Results and Discussion

3.1. X-ray Diffraction (XRD) Patterns of the Mo-Ag Films with Different Annealing Temperature

The XRD patterns of the Mo-Ag films before and after annealing are shown in Figure 1. The as-deposited Mo-Ag films exhibit weak diffraction peaks in the XRD pattern, inferring fine grains or amorphous structures in the Mo-Ag films at room temperature [30]. Compared with the as-deposited Mo-Ag films, the intensity of the Ag (111) diffraction peaks in the Mo-Ag films annealed at 260 °C and 360 °C increased obviously. The parameters of crystallites in the films annealed at different temperatures is calculated by the Bragg equation ($2d \sin \theta = k\lambda$) and Scherrer formula ($D = \frac{0.89\lambda}{\beta \cos \theta}$). The calculated results of the Ag (111) diffraction peaks are listed in Table 1, indicating that annealing can promote the slow growth of Ag grains. Conversely, the intensity of the Mo (110) diffraction peaks in the Mo-Ag films decreases as the annealing temperature increases, which demonstrated that the Ag grains have an inhibitory effect on the growth of Mo grains [28]. Additionally, there are no diffraction peaks of Mo and Ag compounds in XRD patterns due to the extremely low solubility of Mo and Ag [31].

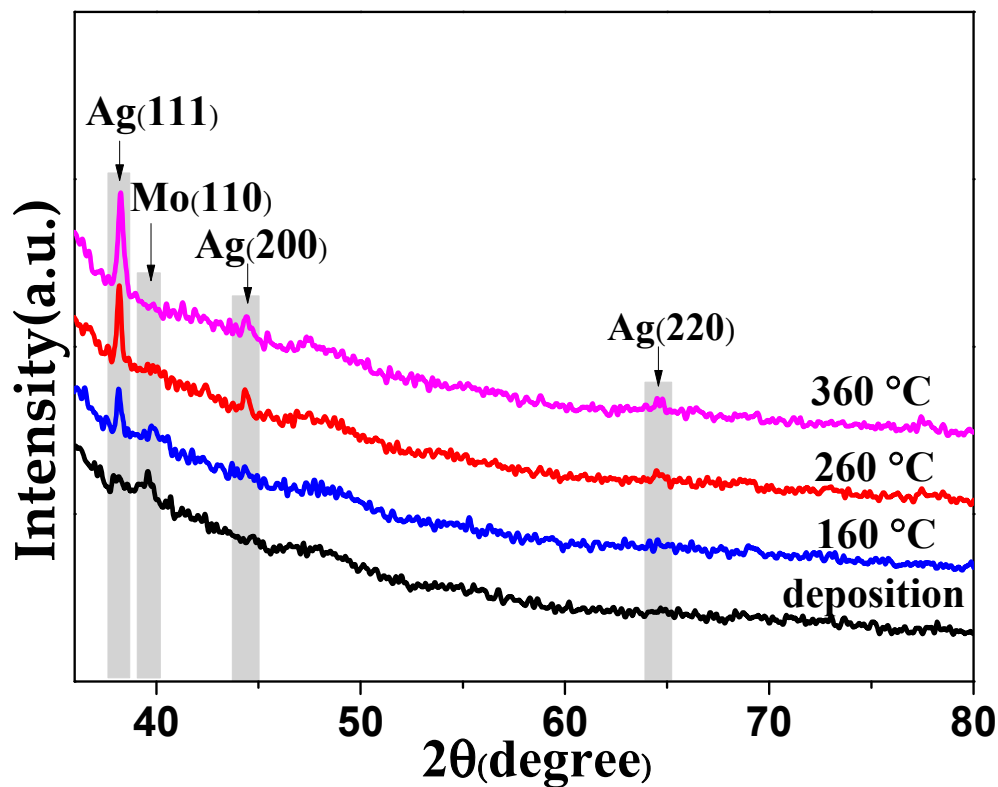


Figure 1. X-ray diffraction (XRD) patterns of the Mo-Ag films before and after annealing.

Table 1. The parameters of crystallites in the films annealed at different temperatures.

Annealing Temperature	2θ (Degree)	d (Å)	β (Degree)	D (nm)
Room temperature	39.573	2.275	0.319	26
160	38.250	2.351	0.268	31
260	38.148	2.357	0.258	32
360	38.271	2.350	0.249	33

The X-ray wavelength λ is 0.15406 nm and the Bragg diffraction angle is θ . Interplanar spacing, full width at half maximum and mean dimension of crystallites are represented by d , β , and D , respectively.

3.2. Morphology Characterization of Annealed Mo-Ag Films

Figure 2 shows the scanning electron microscope (SEM) images of the Mo-Ag films before and after annealing. It can be seen from Figure 2a that a large number of irregular nanoparticles grew on the as-deposited Mo-Ag films' surface. Based on the previous transmission electron microscopy (TEM) and EDS analysis of the self-grown particles on the Mo-Ag films' surface, it can be determined that these particles are Ag particles [28,30]. The structure of Ag particles/Mo-Ag films/PI is similar to that of Ag clusters/Si. However, the preparation condition and formation mechanism of Ag particles are completely different from Ag nanoclusters [17]. According to EDS analysis, the composition of Ag and Mo in the Mo-Ag film are 48.2% and 51.8%, respectively. The morphology and size of Ag particles on the annealed Mo-Ag film is obviously different from those on the as-deposited Mo-Ag film, as shown in Figure 2a–d. Compared with the Ag particles on the as-deposited Mo-Ag film, the size of Ag particles on the Mo-Ag film annealed at 160 °C is increased by 28 nm and the morphology becomes more regular. As annealing temperature rises to 260 °C and 360 °C, Ag particles have grown into polyhedrons with sharp edges and corners, as shown in Figure 2c,d. Meanwhile, the size and number of polyhedral particles have greatly increased because Ag atoms diffuse more actively. In addition, the composition of the Mo-Ag film before and after annealing is basically unchanged according to the EDS analysis in Figure 2d. Figure 2e₁ is the element mapping of the Mo-48.2% Ag film annealed at

360 °C in Figure 2e. Figure 2e₂,e₃ show that element mapping of Mo and Ag distributed uniformly in the Mo-48.2% Ag film, respectively. Moreover, Figure 2e₃ shows that the particles on the annealed 360 °C Mo-48.2% Ag film are Ag particles, which is consistent with the previous studies of as-deposited Mo-Ag film [28]. Because of the mutual inhibition of Mo and Ag grains in the Mo-Ag films [30,32], the distortion energy and residual stress are released through sufficient mass transport during the annealing process to form plenty of polyhedral particles on the Mo-48.2% Ag films.

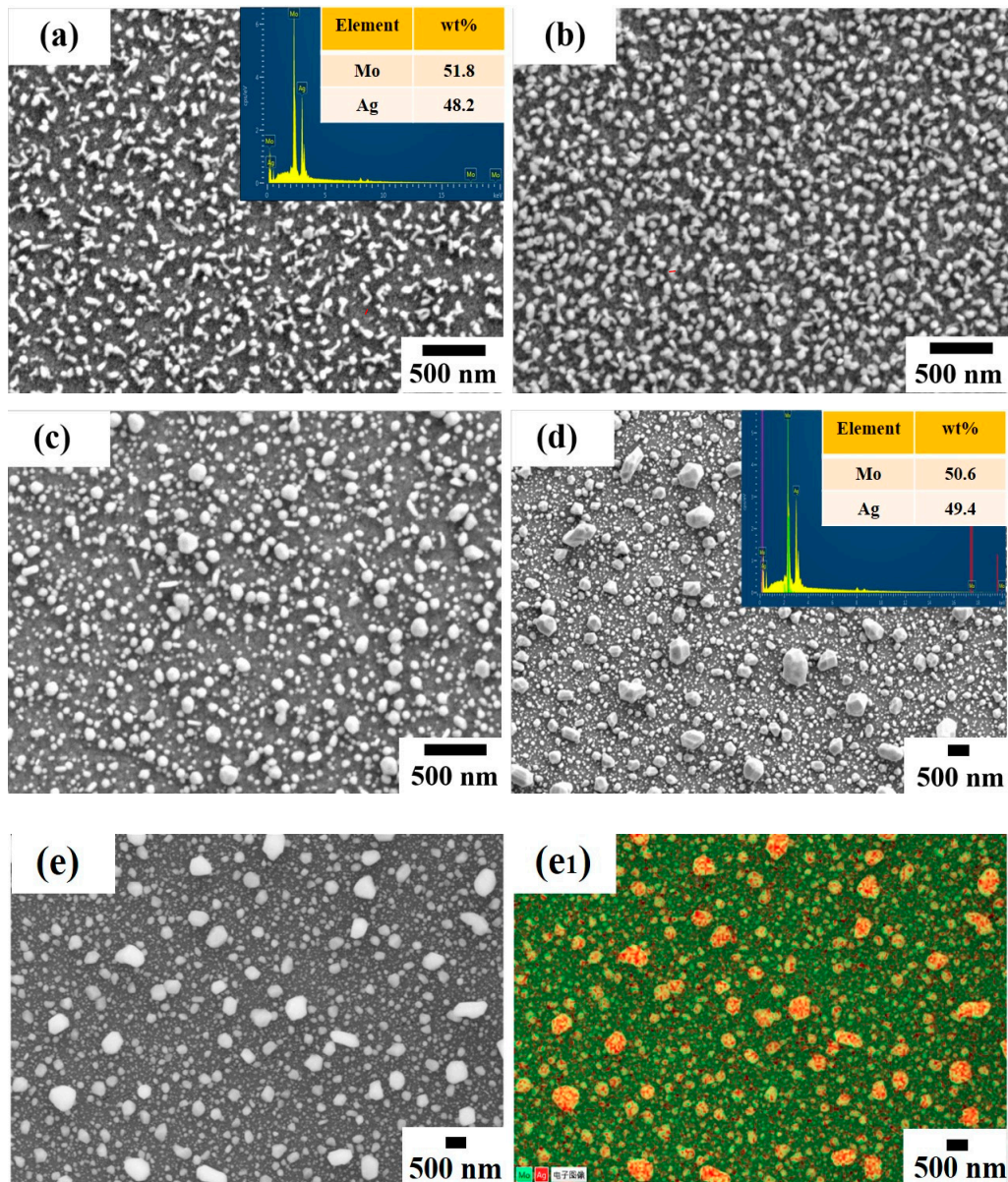


Figure 2. Cont.

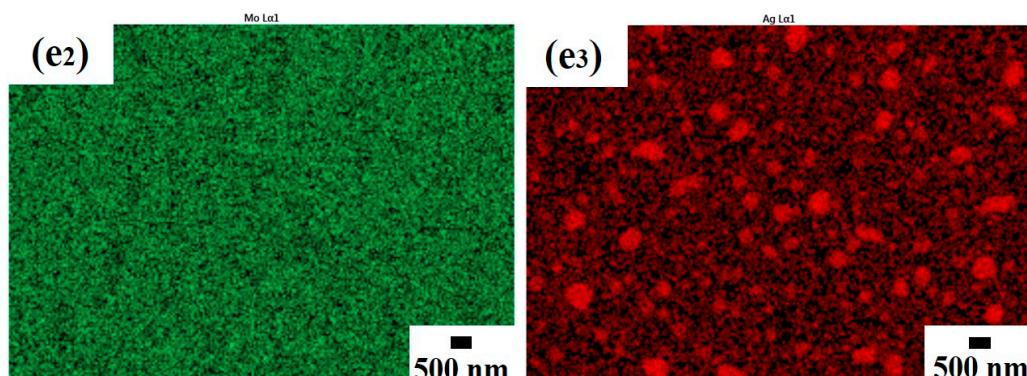


Figure 2. The scanning electron microscope (SEM) images of the Mo-48.2% Ag films before and after annealing: (a) room temperature; (b) 160 °C; (c) 260 °C; (d) 360 °C; (e) the electronic image of Figure 2d; (e₁) element mapping of Figure 2e; (e₂) Mo mapping of Figure 2e₁; (e₃) Ag mapping of Figure 2e₁.

3.3. Preparation and Raman Measurement of the Ag Layer/Annealed Mo-48.2% Ag Film

Figure 3 is a schematic diagram of the formation of Ag particles on the Mo-48.2% Ag film. The Mo-48.2% Ag films were prepared on PI substrates at room temperature, as shown in Figure 3I. According to previous studies [33,34], the internal stress of the film can be released by forming particles on the film. Therefore, numerous “worm-like” particles were formed on the as-deposited Mo-48.2% Ag films. Note that the morphology and size of the Ag particles on the annealed Mo-48.2% Ag films are significantly different from those of the as-deposited Mo-48.2% Ag films because of the stronger diffusion ability of Ag atoms at higher temperature, as shown in Figure 3II. Moreover, as the annealing temperature rises, the morphology of Ag particles changed from irregular particles on the as-deposited Mo-48.2% Ag film to polyhedral particles on the annealed Mo-48.2% Ag film. Simultaneously, the further relaxation of stress in the Mo-48.2% Ag film will grow some new small Ag particles. The formation mechanism of the polyhedral Ag particles on the annealed Mo-Ag alloy film is similar to that of the annealed Ag-Zr alloy film [29], but is different from that of hillocks observed in the Pt/Ti film [35]. An Ag layer can be deposited on the annealed Mo-48.2% Ag films in order to obtain large specific surface area, as shown in Figure 3III. Finally, the CV molecules adsorbed on the Ag layer/annealed Mo-48.2% Ag films are detected by a Raman spectrometer with 532 nm laser wavelength, as shown in Figure 3IV. The laser excitation energy, diffraction grid and spot are 5 mW, 1200 gr/mm and 2 μm, respectively. The scanning range and acquisition time are, respectively, 200–2000 cm⁻¹ and 1 s.

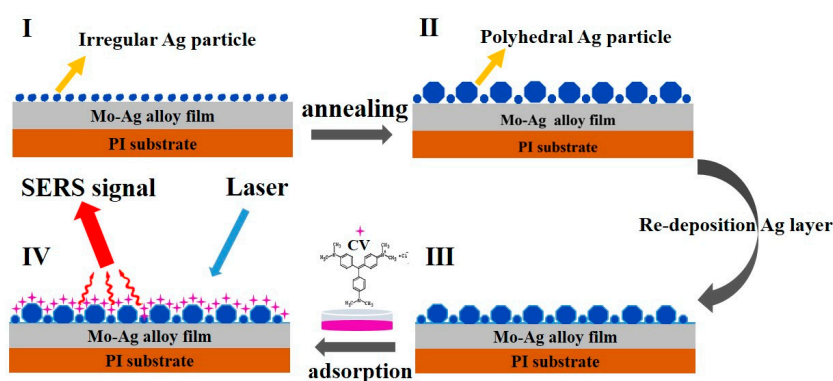


Figure 3. Schematic diagram of the Ag layer/annealed Mo-48.2% Ag film formation: (I) Mo-48.2% Ag films were prepared on PI substrate at room temperature; (II) the Mo-48.2% Ag film annealed in argon atmosphere; (III) an Ag layer was further sputtered on the annealed Mo-48.2% Ag films; (IV) the surface-enhanced Raman scattering (SERS) performance of the Ag layer/annealed Mo-48.2% Ag film was measured.

3.4. Electrical Performance of the Annealed Mo-48.2% Ag Film

Figure 4a–d shows cross-sectional morphology of the Mo-Ag films before and after annealing. Obviously, the Ag particles are distributed on the Mo-48.2% Ag film, and the position relationship between Ag particles and the films is different from the hillock [36]. The thickness of the Mo-48.2% Ag film can be clearly seen from the cross-sectional morphology, and the film thickness gradually decreases as the annealing temperature increases as shown in Figure 4e. The reason is that the formation and growth of polyhedral Ag particles on the annealed Mo-Ag film consumes abundant Ag atoms in the vicinity of the film surface. The square resistance of the Mo-48.2% Ag film was characterized by the four-point probe resistance, and the results are shown in Figure 4f. Meanwhile, the resistivity of the Mo-48.2% Ag films gradually decreases as the annealing temperature rises, which can be ascribed to grain growth and reduction of the defects in the annealed films [37]. Moreover, the decrease of electron scattering in the film promotes the transmission of electrons, which leads to the decrease of resistivity and square resistance of the film.

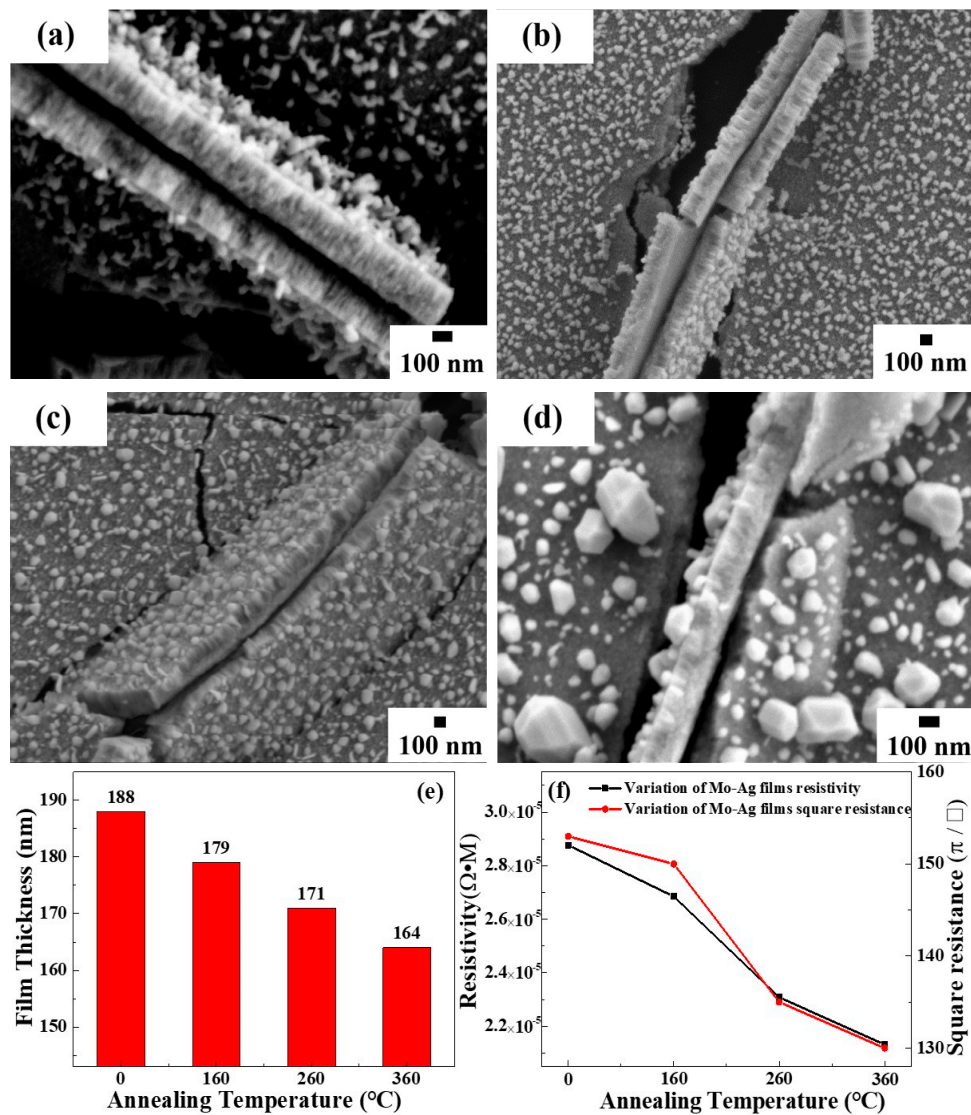


Figure 4. Cross-sectional morphology of Mo-48.2% Ag films annealed before and after annealing: (a) room temperature; (b) 160 °C; (c) 260 °C; (d) 360 °C; (e) variation of the film thickness with annealing temperature; (f) variation of square resistance and resistivity of Mo-48.2% Ag film with annealing temperature.

3.5. Surface-Enhanced Raman Scattering (SERS) Activity of the Ag Layer/Annealed Mo-48.2% Ag Films

Figure 5a is the SEM image of the Mo-48.2% Ag film annealed at 360 °C after further sputtering the Ag layer. Deposition of an Ag layer on the annealed Mo-48.2% Ag film can not only significantly increase the Ag particle size and the surface roughness, but also decrease the gaps between Ag particles. Figure 5b is the FDTD simulation of the EM field intensity in the red circle region of Figure 5a. Obviously, compared with the annealed Mo-48.2% Ag film, the electric field intensity of the Ag layer/annealed Mo-48.2% Ag film is significantly enhanced. This phenomenon confirms that covering an Ag layer on the annealed Mo-48.2% Ag films can increase the number of “hot spots” and cause a near-field enhancement. In order to make the CV fully adsorbed on the SERS substrates, the Ag layer/annealed Mo-48.2% Ag films were soaked in a 10 mL CV solution for 1 h and dried naturally in the air before Raman testing. Figure 5c shows the Raman spectra of CV molecules adsorbed on the Ag layer/Mo-48.2% Ag films with different annealing temperatures, and the fingerprint bands in the spectra of CV molecules are observed [38,39]. Moreover, it is noted from Figure 5c that the Ag layer/Mo-48.2% Ag film annealed at 360 °C has the excellent SERS performance. Therefore, to further determine the SERS sensitivity of the Ag layer/Mo-48.2% Ag film annealed at 360 °C as SERS substrates, the SERS substrates were soaked in 5×10^{-6} , 5×10^{-7} , 5×10^{-8} , 5×10^{-9} and 5×10^{-10} M CV solutions, respectively. Note that SERS spectra in Figure 5d show that Raman spectrum of CV solution with concentration of 10^{-10} M could still be clearly discerned successfully. In addition, the enhancement factor (EF) can be accurately calculate by following formula [40]:

$$EF = \frac{I_{SERS} / C_{SERS}}{I_{Raman} / C_{Raman}} = \frac{I_{SERS}}{I_{Raman}} \times \frac{C_{Raman}}{C_{SERS}} = \frac{2376.216}{46.389} \times \frac{10^{-3}}{10^{-10}} = 5.12 \times 10^8 \quad (1)$$

where I_{SERS} and I_{Raman} are the integrated intensities of the SERS signal of the Ag layer/Mo-48.2% Ag film (1622 cm^{-1}) and pure PI substrate, respectively. C_{SERS} and C_{Raman} are the concentrations of CV adsorbed on the Ag layer/Mo-48.2% Ag film and PI substrate, respectively. The Ag layer/Mo-48.2% Ag films annealed at 360 °C as SERS substrates exhibit preeminent SERS activity to CV molecules, and the enhancement factor can reach 5.12×10^8 . In order to verify the repeatability of the Ag layer/Mo-48.2% Ag films as SERS substrates, we randomly selected 20 different points on the same sample for Raman testing, and the results are shown in Figure 5e. Additionally, the strongest characteristic peaks at 1622 cm^{-1} in the CV molecular spectrum were selected to evaluate the repeatability of the SERS substrate, as shown in Figure 5f. Obviously, the intensity of the Ag layer/Mo-48.2% Ag film at 20 points of the 1622 cm^{-1} peaks with 5×10^{-8} M CV solutions is very close to 8000, which indicates that the film has good uniformity and repeatability.

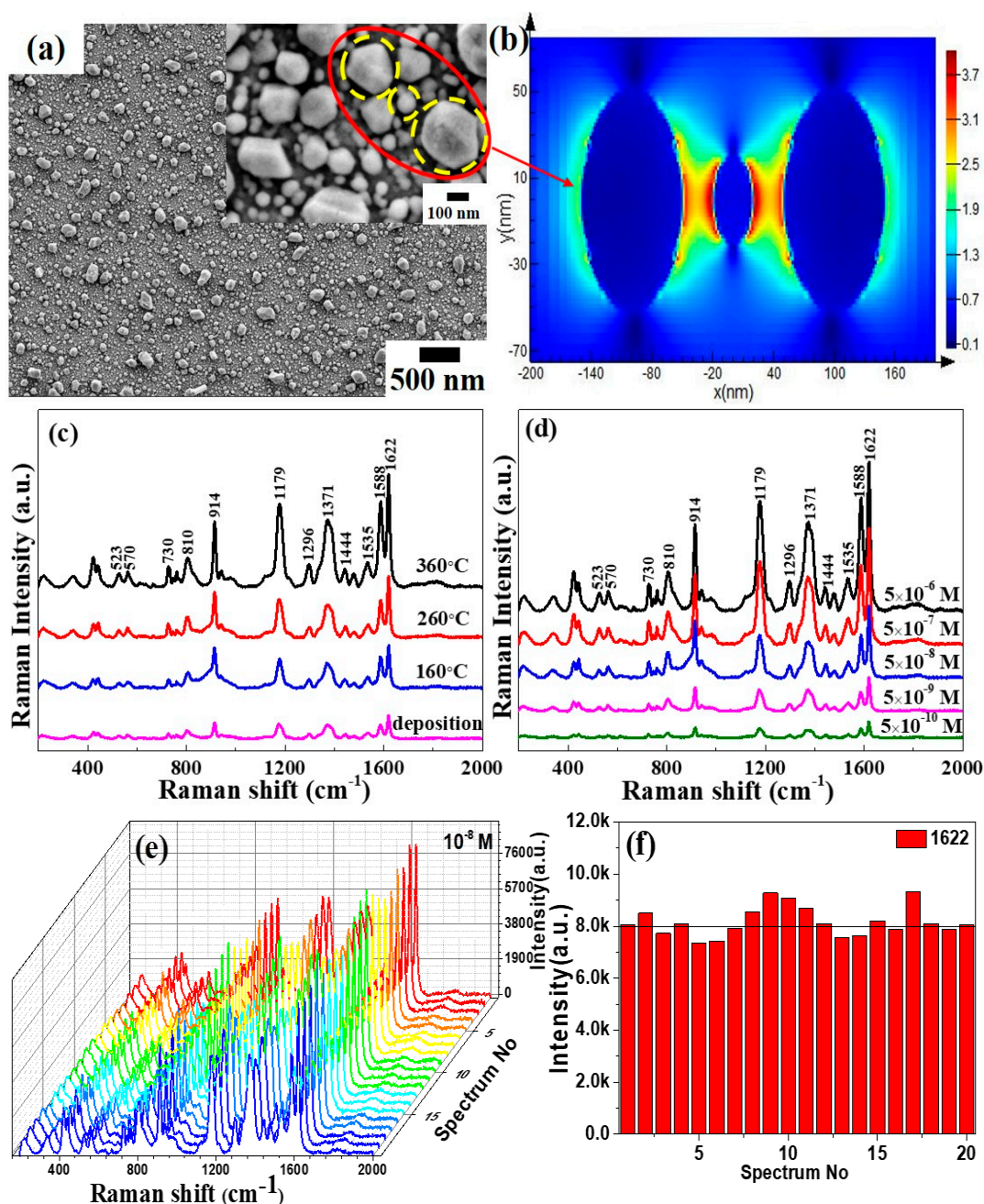


Figure 5. (a) SEM image of the Ag layer/Mo-48.2% Ag films annealed at 360 °C; (b) finite-difference time-domain (FDTD) simulations of the EM field intensity in the red circle region of Figure (a); (c) SERS spectra of the Ag layer/Mo-48.2% Ag films with different annealing temperatures; (d) SERS spectra of the Ag layer/Mo-48.2% Ag films annealed at 360 °C in different concentrations of CV solution; (e) SERS spectra of 20 randomly selected locations in the Ag layer/Mo-48.2% Ag films annealed at 360 °C; (f) variation of the Raman spectra intensity at 1622 cm⁻¹ peaks in (e).

4. Conclusions

Ag layer/annealed Mo-48.2% Ag films were fabricated on PI substrate by DC magnetron sputtering and atmosphere annealing. The Ag particles on the as-deposited Mo-48.2% Ag films are irregular, but the Ag particles on the annealed Mo-48.2% Ag film are gradually transformed into polyhedrons with sharp edges and corners. Moreover, the film thickness and resistivity gradually decrease as the annealing temperature increases. Furthermore, covering an Ag layer on the annealed Mo-48.2%

Ag film can not only significantly increase the Ag particle size and the surface roughness, but also decrease the gaps between Ag particles, resulting in a significant enhancement of the local EM field. The Ag layer/Mo-48.2% Ag films annealed at 360 °C as SERS substrates show high sensitivity of the enhancement factor (EF) up to 5.12×10^8 with the detection limit concentration of CV lower than 10^{-10} M. As a high-sensitivity fingerprint identification tool, the Ag layer/Mo-48.2% Ag films as SERS substrates have shown great application potential in biomedicine, environmental monitoring, food and drug safety and other fields.

Author Contributions: Conceptualization, H.S. and G.W.; methodology, X.L. and H.S.; software, Y.L. (Yuanjiang Lv) and C.X.; validation, X.L. and Y.L. (Yuanjiang Lv); Investigation, Y.L. (Yuanhao Liu), J.D. and Y.W.; formal analysis, X.L.; resources, H.S. and G.W.; Visualization, X.L. and H.S.; data curation, X.L.; writing—Original draft preparation, X.L.; writing—Review and editing, H.S. and X.L.; supervision, H.S.; project administration, H.S.; funding acquisition, H.S. and G.W. All authors have read and agreed to the published version of the manuscript.

Funding: This research was funded by the National Natural Science Foundation of China, grant number U12041869, the Chinese 02 Special Fund, grant number 2017ZX02408003 and National Undergraduate Entrepreneurship Training Program, grant number 202010464013.

Conflicts of Interest: The authors declare no conflict of interest.

References

1. Lee, C.H.; Hankus, M.E.; Tian, L.; Pellegrino, P.M.; Singamaneni, S. Highly sensitive surface enhanced Raman scattering substrates based on filter paper loaded with plasmonic nanostructures. *Anal. Chem.* **2011**, *83*, 8953–8958. [[CrossRef](#)] [[PubMed](#)]
2. Langer, J.; Aberasturi, D.J.D.; Aizpuru, J.; Alvarez-Puebla, R.A.; Auguie, B.; Baumberg, J.J.; Bazan, G.C.; Bell, S.E.J.; Boisen, A.; Brolo, A.G.; et al. Present and Future of Surface Enhanced Raman Scattering. *ACS Nano* **2020**, *14*, 28–117. [[CrossRef](#)] [[PubMed](#)]
3. Sun, D.; Qi, G.; Xu, S.; Xu, W. Construction of high sensitive surface-enhanced Raman scattering (SERS) nanosensor aimed for the test of glucose in urine. *RSC Adv.* **2016**. [[CrossRef](#)]
4. Wang, T.; Zhou, J.; Wang, Y. Simple, Low-Cost Fabrication of Highly Uniform and Reproducible SERS Substrates Composed of Ag–Pt Nanoparticles. *Nanomaterials* **2018**, *8*, 331. [[CrossRef](#)] [[PubMed](#)]
5. Polavarapu, L.; Liz-Marzán, L.M. Towards low-cost flexible substrates for nanoplasmonic sensing. *Phys. Chem. Chem. Phys.* **2013**, *15*, 5288. [[CrossRef](#)]
6. Fei, X.; Liu, Z.; Hou, Y.; Li, Y.; Yang, G.; Su, C.; Wang, Z.; Zhong, H.; Zhuang, Z.; Guo, Z. Synthesis of Au NP@MoS₂ Quantum Dots Core@Shell Nanocomposites for SERS Bio-Analysis and Label-Free Bio-Imaging. *Materials* **2017**, *10*, 650. [[CrossRef](#)]
7. Tseng, S.C.; Yu, C.C.; Wan, D.; Chen, H.L.; Wang, L.A.; Wu, M.C.; Su, W.F.; Han, H.C.; Chen, L.C. Eco-Friendly Plasmonic Sensors: Using the Photothermal Effect to Prepare Metal Nanoparticle-Containing Test Papers for Highly Sensitive Colorimetric Detection. *Anal. Chem.* **2012**, *84*, 5140. [[CrossRef](#)]
8. Zhang, C.; Huang, Q.; Cui, Q.; Ji, C.; Zhang, Z.; Chen, X.; George, T.; Zhao, S.; Guo, L.J. High-Performance Large-Scale Flexible Optoelectronics Using Ultrathin Silver Films with Tunable Properties. *ACS Appl. Mater. Interfaces* **2019**, *11*. [[CrossRef](#)]
9. Leopold, N.; Lendl, B. A New Method for Fast Preparation of Highly Surface-Enhanced Raman Scattering (SERS) Active Silver Colloids at Room Temperature by Reduction of Silver Nitrate with Hydroxylamine Hydrochloride. *J. Phys. Chem. B* **2003**, *107*, 5723–5727. [[CrossRef](#)]
10. Ambroziak, R.; Hodyński, M.; Pociński, T.; Pisarek, M.; Kudelski, A. Cubic Silver Nanoparticles Fixed on TiO₂ Nanotubes as Simple and Efficient Substrates for Surface Enhanced Raman Scattering. *Materials* **2019**, *12*, 3373. [[CrossRef](#)]
11. Yang, C.; Xiang, X.; Zhang, Y.; Peng, Z.; Cao, Z.; Wang, J.; Xuan, L. Large-scale controlled fabrication of highly roughened flower-like silver nanostructures in liquid crystalline phase. *Sci. Rep.* **2015**, *5*, 12355. [[CrossRef](#)] [[PubMed](#)]
12. Lee, S.W.; Chang, S.H.; Lai, Y.S.; Lin, C.C.; Tsai, C.M.; Lee, Y.C.; Chen, J.C.; Huang, C.L. Effect of Temperature on the Growth of Silver Nanoparticles Using Plasmon-Mediated Method under the Irradiation of Green LEDs. *Materials* **2014**, *7*, 7781–7798. [[CrossRef](#)]

13. Tao, A.; Kim, F.; Hess, C.; Goldberger, J.; He, R.; Sun, Y.; Xia, Y.; Yang, P. Langmuir–Blodgett Silver Nanowire Monolayers for Molecular Sensing Using Surface-Enhanced Raman Spectroscopy. *Nano Lett.* **2003**, *3*, 1229–1233. [[CrossRef](#)]
14. Yang, Y.; Li, Z.Y.; Yamaguchi, K.; Tanemura, M.; Huang, Z.; Jiang, D.; Chen, Y.; Zhou, F.; Nogami, M. Controlled fabrication of silver nanoneedles array for SERS and their application in rapid detection of narcotics. *Nanoscale* **2012**, *4*, 2663–2669. [[CrossRef](#)] [[PubMed](#)]
15. Singh, J.P.; Chu, H.Y.; Abell, J.; Tripp, R.A.; Zhao, Y. Flexible and mechanical strain resistant large area SERS active substrates. *Nanoscale* **2012**, *4*, 3410–3414. [[CrossRef](#)]
16. Wang, K.; Sun, D.W.; Pu, H.; Wei, Q.Y.; Huang, L. A Stable, Flexible and High-Performance SERS Chip Enabled by Ternary Films-Packaged Plasmonic Nanoparticles Array. *ACS Appl. Mater. Interfaces* **2019**, *11*. [[CrossRef](#)]
17. Bhattacharyya, S.R.; Datta, D.; Shyjumon, I.; Smirnov, B.M.; Chini, T.K.; Ghose, D.; Hippler, R. Growth and melting of silicon supported silver nanocluster films. *J. Phys. D Appl. Phys.* **2009**, *42*, 035306. [[CrossRef](#)]
18. Tao, A.; Sinsermsuksakul, P.; Yang, P. Polyhedral silver nanocrystals with distinct scattering signatures. *Angew. Chem.* **2010**, *45*, 4597–4601. [[CrossRef](#)]
19. Zhang, R.; Xu, B.B.; Liu, X.Q.; Zhang, Y.L.; Xu, Y.; Chen, Q.D.; Sun, H.B. Highly efficient SERS test strips. *Chem. Commun.* **2012**, *48*, 5913–5915. [[CrossRef](#)]
20. Xu, B.B.; Ma, Z.C.; Wang, H.; Liu, X.Q.; Zhang, Y.L.; Zhang, X.L.; Zhang, R.; Jiang, H.B.; Sun, H.B. A SERS-active microfluidic device with tunable surface plasmon resonances. *Electrophoresis* **2011**, *32*, 3378–3384. [[CrossRef](#)]
21. Ma, Y.; Yang, L.; Yang, Y.; Peng, Y.; Wei, Y.; Huang, Z. Multifunctional Ag-decorated g-C₃N₄ nanosheets as recyclable SERS substrates for CV and RhB detection. *RSC Adv.* **2018**, *8*, 22095. [[CrossRef](#)]
22. Zhu, S.Q.; Zhang, T.; Guo, X.L.; Wang, L.D. Self-Assembly of Two-Dimensional Hexagon Shaped Gold Nanoparticle Film Using Solvent Evaporation Method. *Nanosci. Nanotechnol. Lett.* **2013**, *5*, 253–256. [[CrossRef](#)]
23. Bozzini, B.; Gaudenzi, G.P.D.; Mele, C. A SERS investigation of the electrodeposition of Ag–Au alloys from free-cyanide solutions. *J. Electroanal. Chem.* **2004**, *570*, 29–34. [[CrossRef](#)]
24. Mahato, M.; Sarkar, R.; Pal, P.; Talapatra, G.B. Formation of silver nanoparticle at phospholipid template using Langmuir–Blodgett technique and its Surface-enhanced Raman Spectroscopy application. *Indian J. Phys.* **2015**, *89*, 997–1005. [[CrossRef](#)]
25. Fasolato, C.; Domenici, F.; Brasili, F.; Mura, F.; Sennato, S.; Angelis, D.L.; Mazzi, E.; Bordi, F.; Postorino, P. Self-Assembled Nanoparticle Aggregates: Organizing Disorder for High Performance Surface-Enhanced Spectroscopy. *AIP Conf. Proc.* **2015**. [[CrossRef](#)]
26. Zhu, W.; Wu, Y.; Yan, C.; Wang, C.; Zhang, M.; Wu, Z. Facile Synthesis of Mono-Dispersed Polystyrene (PS)/Ag Composite Microspheres via Modified Chemical Reduction. *Materials* **2013**, *6*, 5625–5638. [[CrossRef](#)]
27. Kim, S.M.; Lee, T.; Gil, Y.G.; Kim, G.H.; Park, C.; Jang, H.; Min, J. Fabrication of Bioprobe Self-Assembled on Au–Te Nanoworm Structure for SERS Biosensor. *Materials* **2020**, *13*, 3234. [[CrossRef](#)]
28. Lian, X.X.; Sun, H.L.; Lv, Y.J.; Wang, G.X. Room temperature self-assembled Ag nanoparticles/Mo-37.5% Ag film as efficient flexible SERS substrate. *Mater. Lett.* **2020**. [[CrossRef](#)]
29. Huang, X.X.; Sun, H.L.; Wang, G.X.; Stock, H.R. Self-formation of Ag particles/Ag-Zr alloy films on flexible polyimide as SERS substrates. *Appl. Surf. Sci.* **2019**, *487*, 1341–1347. [[CrossRef](#)]
30. Lian, X.X.; Lv, Y.J.; Sun, H.L.; Hui, D.; Wang, G.X. Effects of Ag contents on the microstructure and SERS performance of self-grown Ag nanoparticles/Mo–Ag alloy films. *Nanotechnol. Rev.* **2020**, *9*, 751–759. [[CrossRef](#)]
31. Sarakinos, K.; Greczynski, G.; Elofsson, V.; Magnfält, D.; Högberg, H.; Alling, B. Theoretical and experimental study of metastable solid solutions and phase stability within the immiscible Ag–Mo binary system. *J. Appl. Phys.* **2016**, *119*, 095303. [[CrossRef](#)]
32. Sun, H.L.; Huang, X.X.; He, M.J.; Lian, X.X.; Wang, G.X. Preparation and controllability of Cu particles on annealed Mo–Cu alloy films. *Mater. Lett.* **2019**, *254*, 175–177. [[CrossRef](#)]
33. Sun, H.L.; Huang, X.X.; Lian, X.X.; Wang, G.X. Discrepancies in the Microstructures of Annealed Cu–Zr Bulk Alloy and Cu–Zr Alloy Films. *Materials* **2019**, *12*, 2467. [[CrossRef](#)] [[PubMed](#)]
34. Sun, H.L.; Huang, X.X.; Lian, X.X.; Wang, G.X. Adjustment Cu₃Si growth in the interface of annealed Cu–Zr alloy films/Si substrate to form inverted pyramid structure. *Mater. Lett.* **2019**. [[CrossRef](#)]

35. Kweon, S.Y.; Choi, S.K.; Yeom, S.J.; Roh, J.S. Platinum Hillocks in Pt/Ti Film Stacks Deposited on Thermally Oxidized Si Substrate. *Jpn. J. Appl. Phys.* **2001**, *40*, 5850–5855. [[CrossRef](#)]
36. Chen, C.; Suganuma, K. Low temperature SiC die-attach bonding technology by hillocks generation on Al sheet surface with stress self-generation and self-release. *Sci. Rep.* **2020**, *10*. [[CrossRef](#)]
37. Huang, X.X.; Sun, H.L.; Shen, J.; Cui, K.; Wang, G.X. Different Effects of Annealing on Microstructure Evolution and SERS Performance for Cu-Cr Alloy Film and Bulk Alloy. *Materials* **2019**, *12*, 2990. [[CrossRef](#)]
38. Ding, Q.; Zhang, L.; Yang, L. A simple approach for the synthesis of Ag-coated Ni@TiO₂ nanocomposites as recyclable photocatalysts and SERS substrate to monitor catalytic degradation of dye molecules. *Mater. Res. Bull.* **2014**, *53*, 205–210. [[CrossRef](#)]
39. Zhang, K.; Zeng, T.; Tan, X.; Wu, W.; Tang, Y.; Zhang, H. A facile surface-enhanced Raman scattering (SERS) detection of rhodamine 6G and crystal violet using Au nanoparticle substrates. *Appl. Surf. Sci.* **2015**, *347*, 569–573. [[CrossRef](#)]
40. Stiles, P.L.; Dieringer, J.A.; Shah, N.C.; Van Duyne, R.P. Surface-enhanced Raman spectroscopy. *Annu. Rev. Anal. Chem.* **2008**, *1*, 601–626. [[CrossRef](#)]



© 2020 by the authors. Licensee MDPI, Basel, Switzerland. This article is an open access article distributed under the terms and conditions of the Creative Commons Attribution (CC BY) license (<http://creativecommons.org/licenses/by/4.0/>).